

Magnetic properties of epitaxial CoCr films with depth-dependent exchange-coupling profilesLorenzo Fallarino,¹ Brian J. Kirby,² Matteo Pancaldi,¹ Patricia Riego,^{1,3} Andrew L. Balk,^{4,5} Casey W. Miller,^{6,7} Paolo Vavassori,^{1,8} and Andreas Berger¹¹*CIC nanoGUNE Consolider, Tolosa Hiribidea 76, E-20018 Donostia-San Sebastian, Spain*²*Center for Neutron Research, National Institute of Standards and Technology, Gaithersburg, Maryland 20899, USA*³*Departamento de Física de la Materia Condensada, Universidad del País Vasco, UPV/EHU, E-48080 Bilbao, Spain*⁴*Center for Nanoscale Science and Technology, National Institute of Standards and Technology, Gaithersburg, Maryland 20899, USA*⁵*Maryland Nanocenter, University of Maryland, College Park, Maryland 20742, USA*⁶*School of Chemistry and Materials Science, Rochester Institute of Technology, Rochester, New York, USA*⁷*Department of Physics, University of Gothenburg, 412 96 Gothenburg, Sweden*⁸*IKERBASQUE, Basque Foundation for Science, E-48013 Bilbao, Spain*

(Received 2 November 2016; revised manuscript received 23 February 2017; published 27 April 2017)

We present a study of the compositional and temperature-dependent magnetic properties of epitaxial CoCr thin films whose composition has a bathtublike depth profile $\text{Co}/\text{Co}_{1-x_c}\text{Cr}_{x_c}/\text{Co}_{1-x_c}\text{Cr}_{x_c}/\text{Co}_{1-x_c}\text{Cr}_{x_c}\rightarrow 0/\text{Co}$ with the highest Cr concentration (x_c) at the center of the sample. Polarized neutron reflectometry (PNR) shows that the effective Curie temperature varies as a function of depth and exhibits a minimum in the center of the structure. Correspondingly, we observe that the effective coupling between the two outer Co layers is strongly dependent on the magnetization of the graded CoCr spacer and can be continuously tuned via x_c and temperature T . In particular, for $x_c = 0.28$, magnetometry reveals a transition from one-step to two-step reversal behavior for temperatures $T > 260$ K, indicating a transition from a fully correlated magnetic film structure to an uncoupled system containing effectively two independent magnetic sublayers. Corroborating evidence of the temperature-dependent coupling of the top and bottom regions for $x_c = 0.28$ was revealed by PNR, which demonstrated the field-dependent occurrence of antiparallel magnetization alignment on opposite interfaces at sufficiently high temperatures only.

DOI: [10.1103/PhysRevB.95.134445](https://doi.org/10.1103/PhysRevB.95.134445)**I. INTRODUCTION**

Multilayer structures made from metallic magnetic and nonmagnetic materials have revealed an impressive variety of novel collective properties, and they now represent an established and very successful approach to materials design with widespread applications [1,2]. The overall magnetic ordering in these artificial structures strongly depends on the interlayer and the intralayer couplings, and the corresponding basic magnetic properties, such as Curie temperature (T_C) or saturation magnetization (M_S), as well as the specifics of the multilayer dimensions [3–6]. Indeed, if the individual layers are sufficiently thick, their properties are bulklike, and the multilayer corresponds to a simple superposition of separate layers. As they get thinner, the magnetic properties of those layers converge and the multilayer behaves as a single new artificial material. One such example, in the limit of magnetic films in direct contact, are exchange spring permanent magnets in which low-moment magnetically hard and high-moment magnetically soft layers are strongly coupled at the interfaces. As a consequence, the maximum energy product in this system is far enhanced in comparison to those of the constituent materials, if the geometry is properly designed [7–14].

This route to novel materials design has recently been taken further, with the accomplishment of a magnetic anisotropy gradient along the thickness of multilayer structures [15–20]. The key goal was hereby the decrease of the switching field (H_S) down to very small values while maintaining thermal stability for the purpose of fulfilling the ever-increasing demands of magnetic recording technology, and doing this by creating a new metamaterial with novel collective behavior. The fabrication of such graded media has historically been based on multilayered structures [21–27] in which extended

interfaces are created by either directly tuning the thicknesses of the magnetic layers [22,24,25] or by interdiffusion via heat treatment [21,23,26,27]. Additionally, the realization of a continuous anisotropy gradient was achieved in optimally postdeposition annealed, compositionally graded single-layer films [28–32]. Furthermore, depth-sensitive polarized neutron reflectivity (PNR) measurements allowed for a direct probing of the corresponding anisotropy gradient behavior [24,25,27–32]. The recently reported work in Ref. [33] demonstrated that not only can an anisotropy gradient be realized and tailored in compositionally graded single-layer films, but the authors also disclosed an effective way to engineer phase transitions and ferromagnetic phase boundaries parallel to the sample surface [33]. In fact, the specific sample structure of Ref. [33], a vertically graded $\text{Ni}_x\text{Cu}_{1-x}$ alloy film, revealed the possibility to map the temperature dependence of the ferromagnetic order parameter onto spatial coordinates (i.e., a magnetic depth profile), which can be altered by both temperature and magnetic field. Hereby, one has to consider that, formally, a magnetic material that exhibits ferromagnetic exchange coupling throughout should exhibit only one single T_C . Practically, however, in the presence of pronounced compositional gradients as the one studied in [33], the system can be thought of as having a continuous distribution of “local” or effective T_C , which leads to an effective spatial conversion of the M vs T curve. The resulting depth-dependent T_C modulations were found to occur even at the nanometer-length scale [33], which is a very relevant length scale close to the exchange length (l_{ex}) of elemental ferromagnets and extremely important for applications, because it is fully compatible with the length scale being employed in modern nanotechnology applications.

The main motivation of the present work is to investigate whether and how such effective Curie temperature depth profiles can be utilized to modify collective magnetic behavior, with particular emphasis on magnetization reversal. Indeed, rationally designed composition profiles can be envisioned to achieve desired temperature and field dependencies by facilitating complex collective or noncollective magnetic behavior. This may also have relevance for temperature-assisted magnetic recording technologies that are presently being explored for hard disk drive (HDD) and magnetic random access memory (MRAM) applications. Here, the triggering of a temperature-induced decoupling of different magnetic properties, namely, magnetic reversibility and stability, is being pursued.

However, the fundamentals of the associated collective or only partially collective behavior will have to be studied first to allow for such applications. Our work here is attempting to make a contribution towards an overall understanding of collective behavior in suitably designed nonuniform materials having epitaxial sample quality. By means of thorough experimental investigations, we intend to elucidate the effect of compositional gradients being transferred into depth-dependent magnetic states in structures that are dominated by only ferromagnetic exchange coupling.

Given this goal, $\text{Co}_{1-x}\text{Cr}_x$ alloys are an interesting model system [34–36] in which magnetic properties can be easily tuned by changing the Cr doping concentration x . Both the Curie temperature T_C and saturation magnetization M_S scale with the Co/Cr ratio, making the latter quantity a useful knob for the continuous tuning of T_C and M_S [33–36]. Moreover, the alloy forms a stable solid solution in a wide range of Cr concentrations while preserving the *hcp* crystal structure characteristic of pure Co. For the present work we designed and studied a series of symmetrically graded samples of the form $\text{Co}(20\text{ nm})/\text{Co}_{1-x_c}\text{Cr}_{x_c}(18\text{ nm})/\text{Co}_{1-x_c}\text{Cr}_{x_c}(30\text{ nm})/\text{Co}_{1-x_c}\text{Cr}_{x_c}(18\text{ nm})/\text{Co}(20\text{ nm})$, with x_c representing the maximum Cr content at the center of the structure, as shown in Fig. 1(a). The simplified nomenclature $\text{Co}/\text{Co}_{1-x}\text{Cr}_x/\text{Co}$ will be used for the remainder of the text, with $\text{Co}_{1-x}\text{Cr}_x$ representing the “bathtublike” compositionally graded structure, which has a total thickness of 66 nm. A key aspect and advantage of our specific sample structure is the fact that they are epitaxial and exhibit uniaxial magnetocrystalline anisotropy in the plane of the film. Moreover, the selected thickness is far smaller than the lateral dimensions, resulting in negligible in-plane demagnetization fields. Correspondingly, the film magnetization is restricted to in-plane orientations only. The samples have, therefore, nearly ideal textbook magnetic behavior, which allows for comprehensive and precise quantitative data analysis and interpretation [37,38]. In contrast to the previous study where a linear composition gradient was employed [33], the symmetrically graded T_C “bathtublike” profile here should allow for a tunable coupling of the two outer cobalt layers via the graded central region, with the coupling strength being dependent on the continuously tunable magnetization profile of the graded region itself [33–36]. In other words, our particular sample structure can be considered as having a nonferromagnetic “spacer” layer at the center whose thickness is continuously variable as a function of temperature. Such a tunable spacer should result in strongly

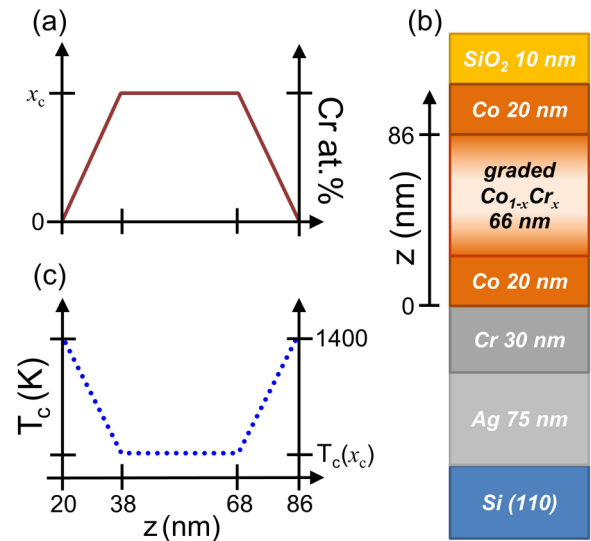


FIG. 1. (a) shows the Cr content depth profile, (b) the schematic of the layer growth sequence for the sample type studied in this work, and (c) the associated effective Curie temperature T_C depth profile for the 66-nm-thick graded $\text{Co}_{1-x}\text{Cr}_x$ layer. $T = 1400$ K corresponds to the T_C of pure cobalt.

temperature-dependent magnetic coupling that significantly influences the magnetization reversal process. It is worth mentioning that a similar temperature dependence might be expected in a more abrupt version of the investigated sample structure, i.e., a basic trilayer $\text{Co}/\text{Co}_{1-x}\text{Cr}_x/\text{Co}$ with the correct stoichiometry and thicknesses. However, the grading of the alloy layer leads to two crucial differences: first, because of the far smoother changes in the magnetization structure, it improves the control of the magnetic properties by means of magnetic field and temperature, leading to a more robust tuning range of the materials properties if compared to a simpler trilayer structure [33]. Second, the graded structure promotes and facilitates the epitaxial growth, because it lowers the epitaxial mismatch that occurs at each interface. The epitaxial growth is crucially important for our experiments here because it enables the realization of in-plane uniaxial anisotropy throughout the magnetic structure.

The paper is organized in the following way: We describe in Sec. II all the experimental methods utilized in the present work; the structural characterization is presented in Sec. III A and our magnetometry studies in Sec. III B. The experimental polarized neutron reflectometry results are discussed in Sec. III C. Section IV summarizes the obtained results and provides the conclusions that can be drawn from them.

II. EXPERIMENTAL METHODS

All samples have been fabricated by means of sputter deposition utilizing a UHV system (ATC series by AJA International) with a base pressure better than 1.2×10^{-6} Pa. Prior to any deposition, the Si (110) substrates were cleaned in organic solvents, rinsed in deionized water, and subsequently etched with hydrofluoric acid (HF). As a result, the native oxide layers and potential surface contaminants were removed. All depositions were performed at room temperature (RT) using a

pressure of 4×10^{-1} Pa of pure Ar atmosphere. Graded layers were fabricated by cosputtering of Co and Cr targets, keeping the power of the former fixed while changing that of the latter to achieve the intended composition profile. An onset layer of 75-nm-thick Ag and a subsequent 30-nm-thick Cr layer were deposited prior to the growth of the magnetic structure in order to achieve a high-quality 20-nm-thick $(10\bar{1}0)$ -oriented Co layer [37–39], which itself served as a template for the epitaxial growth of the 66-nm-thick compositionally graded $\text{Co}_{1-x}\text{Cr}_x$ layer. As a reference, a 106-nm-thick epitaxial pure Co sample ($x_c = 0$) was also fabricated using an identical underlayer sequence. The fabrication of the corresponding “bathtublike” structure was divided into three consecutive steps: the increment of the Cr content up to its maximum x_c was achieved by the stepwise increase of the Cr gun power every 3 nm of deposited film thickness; the central 30-nm-thick $\text{Co}_{1-x_c}\text{Cr}_{x_c}$ layer was deposited keeping the sputter powers of both targets constant; the Cr sputter power was then progressively reduced, again in 3-nm intervals. Afterwards, the 20-nm-thick Co top layer was deposited. The result was a magnetic structure that was nominally symmetric with respect to the center of the depth profile. As a final deposition step, each sample was coated with 10 nm of amorphous SiO_2 in order to avoid any oxidation or contamination. Figure 1(b) shows a schematic of the described growth sequence, optimized to obtain the $(10\bar{1}0)$ orientation throughout the magnetic structure. Consequently, the c axis, which corresponds to the magnetic easy axis (EA) independent from the Cr concentration, lays in the film plane and thus results in a rather simple uniaxial in-plane magnetocrystalline anisotropy, despite the complexity of the sample structure. Using the above growth scheme, we fabricated a series of samples with the maximum dopant concentration at the center of the structure x_c ranging from 0.25 to 0.32. It is worthwhile to mention that for each value of x_c we adapted the Cr concentration of the two linearly increasing and decreasing regions of the sample, i.e., a higher x_c corresponds to a steeper gradient dx/dz . Figure 1(c) illustrates the expected corresponding effective T_C distribution, derived from the combination of the compositional depth profile and the nearly linear relationship between T_C and x [33–36].

The structural analysis of the samples was performed by means of x-ray diffraction (XRD) utilizing a PANalytical X’Pert Pro diffractometer with $\text{Cu } K\alpha$ radiation. The epitaxial orientation relationships and the crystallographic structures have been investigated via XRD θ - 2θ scans, sensitive to the crystal planes parallel to the sample surface, and φ scans, which yield information about the relative orientation of a specific set of diffraction planes.

Room temperature magnetic characterization was performed using a commercial MicroMag 3900 vibrating sample magnetometer (VSM) equipped with a 360° rotational stage that allows for an azimuthal sample orientation alignment with precision of better than 1° . Temperature-dependent magnetization measurements were performed using a commercial Quantum Design MPMS3 SQUID-VSM magnetometer.

Magneto-optical Kerr effect (MOKE) hysteresis loops were measured in the longitudinal configuration at a laser wavelength of $\lambda = 635$ nm in order to obtain a signal proportional

to the in-plane magnetization component lying in the scattering plane, to which we aligned the magnetic EA of each sample as well as the applied magnetic field [40,41]. We also took images of the magnetic domains with a confocal MOKE microscope adjusted to be sensitive to the sample easy magnetization axis. The microscope uses a mercury short arc lamp for illumination, a CCD camera for detection, and a strain-free objective lens with a magnification of $20\times$.

The polarized neutron reflectometry measurements were carried out on the PBR beamline at the NIST Center for Neutron Research. (See Appendix for further details.)

III. RESULTS AND DISCUSSION

A. Structural characterization

A complete structural analysis verifies that our samples have excellent crystallographic quality, with in-plane c -axis orientation over the entire composition range. Figure 2 shows XRD θ - 2θ measurements in the angular range $35^\circ \leq 2\theta \leq 95^\circ$ for several gradient samples that were grown with different maximum Cr concentrations x_c . All the scans look nearly identical in their overall appearance, exhibiting only the well-defined diffraction peaks corresponding to $\text{Si}(220)$, $\text{Ag}(220)$,

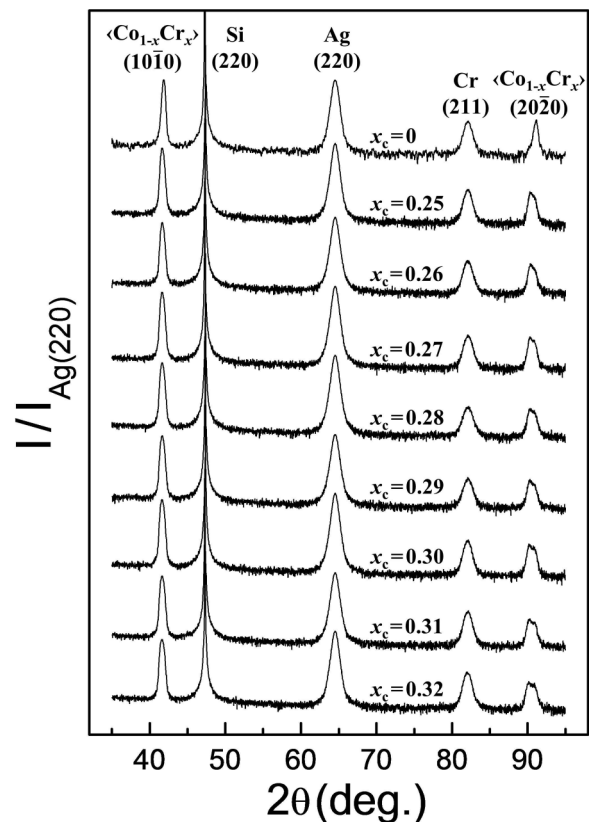


FIG. 2. XRD θ - 2θ scans for different samples with Cr concentrations x_c showing $\langle\text{Co}_{1-x}\text{Cr}_x\rangle$ $(10\bar{1}0)$, $\text{Ag}(220)$, $\text{Cr}(211)$, and $\langle\text{Co}_{1-x}\text{Cr}_x\rangle$ $(20\bar{2}0)$ diffraction peaks, in addition to the $\text{Si}(220)$ substrate signal. Each scan has been normalized to the intensity of its $\text{Ag}(220)$ peak.

Cr(211), $\langle\text{Co}_{1-x}\text{Cr}_x\rangle^1$ (10 $\bar{1}$ 0) and (20 $\bar{2}$ 0) crystal planes. The absence of any other diffraction peak and the fact that higher-order diffraction signals are clearly visible in all the cases are both evident indicators of the excellent crystallographic quality of our samples. In addition, the FWHM and the position of the peaks corresponding to the Ag and Cr seed layers, which serve as templates for the growth of the actual magnetic structures, are identical within the errors in all cases, verifying the robustness of our fabrication process. This also permits us to correlate any significant structural change in the graded layers to the different Cr gradient compositions instead of the variable quality of the template layers. From a global perspective, and as illustrated in Fig. 2, we can assert that all graded samples show an out-of-plane crystallographic orientation quality that is very similar to the 106-nm-thick pure Co reference sample ($x_c = 0$), despite their complex depth-dependent structure.

In contrast to usual x-ray diffraction peaks from homogeneous film, the nature of the peaks corresponding to the $\langle\text{Co}_{1-x}\text{Cr}_x\rangle$ (10 $\bar{1}$ 0) and (20 $\bar{2}$ 0) orientations is quite different and worth discussing further. Each of those Bragg peaks corresponds to a superposition of the signal coming from the two outer Co layers and the signal coming from the interior graded $\text{Co}_{1-x}\text{Cr}_x$ structure. By using a single Gaussian fitting function, the position of the (10 $\bar{1}$ 0) peaks was found to decrease with increasing x_c , whereas the corresponding FWHM increases. Normally, such a peak width increase is associated with a reduced quality of the epitaxial growth. Instead, in compositionally graded samples, it is primarily linked to the superposition of the diffracted x rays from different depths of the modulated structure. Indeed, it is the lattice expansion in the central part of the graded structure that causes the enhanced width of the $\langle\text{Co}_{1-x}\text{Cr}_x\rangle$ (10 $\bar{1}$ 0) peak, changing from 0.46° for the $x_c = 0.25$ sample to 0.57° for the $x_c = 0.32$ structure. This evolution is even clearer for the (20 $\bar{2}$ 0) second-order Bragg reflections, where the overall graded crystallographic structure leads to a splitting of the peak upon increasing x_c . Part of this double-peak structure appears at an angular position close to that of pure Co, which we can attribute to the bottom and top parts of the structure. In contrast, the signal from the central region is shifted to lower diffraction angles, indicating a slight lattice expansion.

Figures 3(a)–3(c) show XRD φ scans for three different maximum Cr concentrations, namely, $x_c = 0.25$, 0.28, and 0.30. The measurements were performed at four different crystal planes that are not parallel to the film surface and thus provide information about the in-plane orientation between the layers. The intensity has been normalized to the maximum value in each corresponding measurement. All φ scans show two well-defined diffraction peaks that are 180° apart and whose positions match the stereographic projection of the nominal epitaxial structure [37]. The 90° angular shift between the Si {004} and Ag {002} scans with respect to the Cr {110} indicates that the Cr [1 $\bar{1}$ 0] and Ag-Si [001] directions are parallel [37]. The $\langle\text{Co}_{1-x}\text{Cr}_x\rangle$ peaks appear at the same

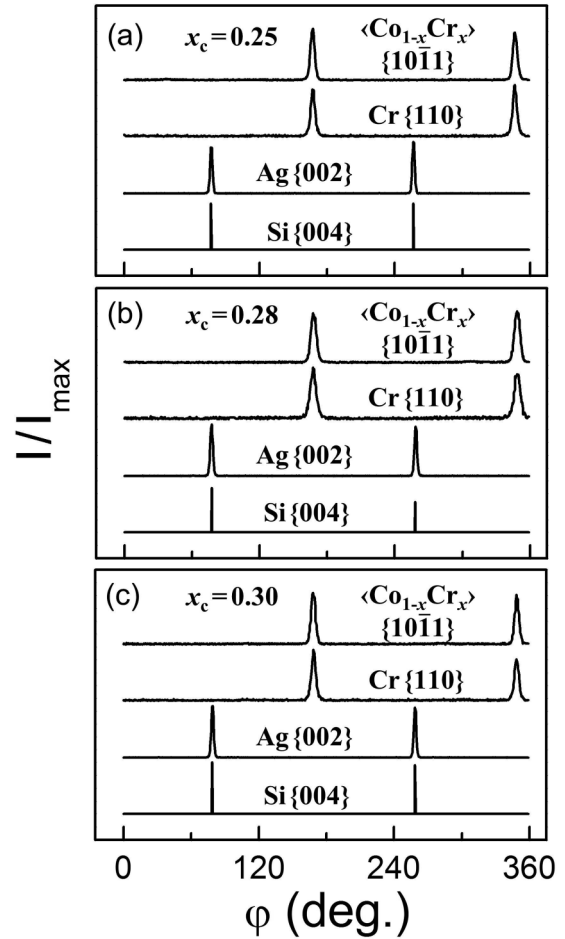


FIG. 3. XRD φ scans at the 2θ poles of the Si {004}, Ag {002}, Cr {110}, and $\langle\text{Co}_{1-x}\text{Cr}_x\rangle$ {10 $\bar{1}$ 1} planes for Cr concentrations $x_c = 0.25, 0.28, 0.30$.

positions as those in the Cr {110} scan, verifying the parallel alignment between the $\langle\text{Co}_{1-x}\text{Cr}_x\rangle$ [0001] and Cr [1 $\bar{1}$ 0] directions. The overall narrow peak widths indicate excellent crystalline order for all samples. Moreover, there is no significant change between the φ scans for different samples, further corroborating the quality and reproducibility of our growth procedure.

The structural analysis of all our samples thus verifies excellent crystallographic quality and well-ordered $\langle\text{Co}_{1-x}\text{Cr}_x\rangle$ graded film exhibiting a uniform in-plane c -axis orientation, which is the EA of magnetization for such alloys in the entire composition range.

B. Magnetic characterization

The macroscopic magnetic properties were analyzed in order to verify that the designed graded structures exhibit the expected uniaxial magnetocrystalline anisotropy with its easy axis in the plane of the film and parallel to the c axis. Figures 4(a)–4(e) display room temperature normalized magnetization M/M_S data as a function of the field strength H and the field angle β , which is defined by the in-plane applied field direction with respect to the crystallographic c axis. The data are shown as color-coded maps for samples

¹In Sec. III A $\langle\text{Co}_{1-x}\text{Cr}_x\rangle$ indicates the Co/ $\text{Co}_{1-x}\text{Cr}_x$ /Co “trilayer” structure.

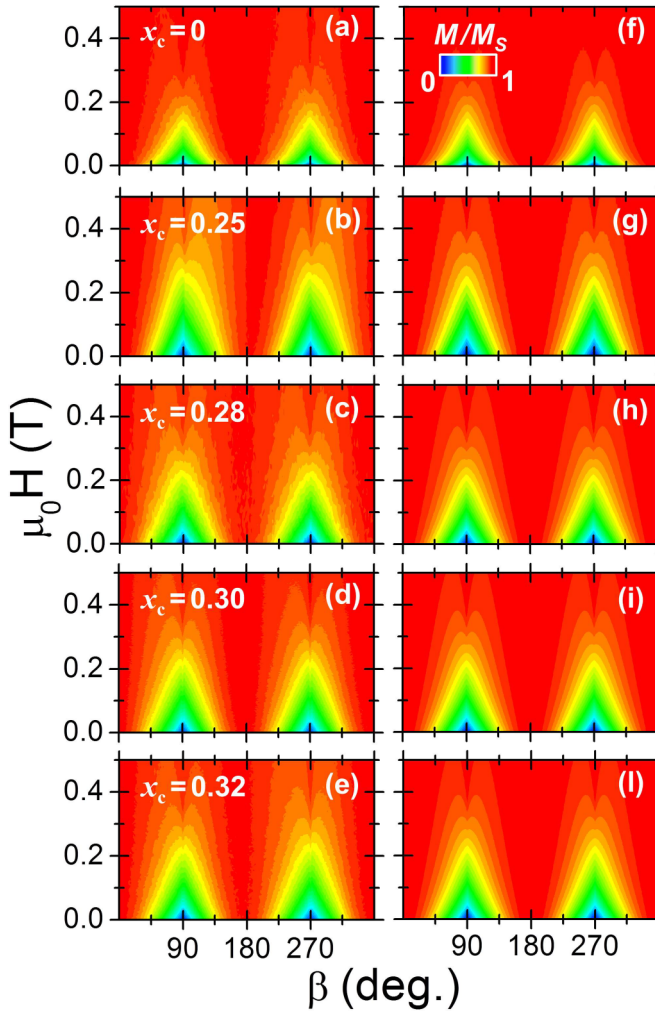


FIG. 4. (a–e) Color-coded maps representing the room temperature in-plane angular dependence of the magnetization measured from saturation to remanence for five samples with different Cr concentrations x_c . The data are normalized to the saturation magnetization M_S evaluated by least-squares fits using Eq. (1) and are plotted as a function of the applied field angle β with respect to the easy axis and the field strength H . (f–l) Corresponding least-squares fits of the data based upon the minimization of the total energy [38].

with $x_c = 0, 0.25, 0.28, 0.30, 0.32$. To assemble these data sets, the magnetization was measured by sweeping the field strength H from positive saturation down to zero at every field orientation angle from $\beta = 0^\circ$ to $\beta = 360^\circ$ using a step size of 2° . All the data show a clear 180° periodicity, with the presence of a cone-shaped structure of reduced magnetization occurring near $\beta = 90^\circ$ and $\beta = 270^\circ$. These cones indeed are expected around the hard axis (HA), because without sufficiently high external magnetic field, the system has negligible magnetization along the field axis. Along $\beta = 0^\circ$ and $\beta = 180^\circ$, the external magnetic field has very little influence on the observed magnetization, because M is saturated along those directions even in the absence of H . These angles correspond to the EA. The experimental maps indicate that all the samples exhibit uniaxial anisotropy with the EA coinciding with the c axis. While the observed behavior is fundamentally identical in all cases, the pure Co reference sample shown in Fig. 4(a)

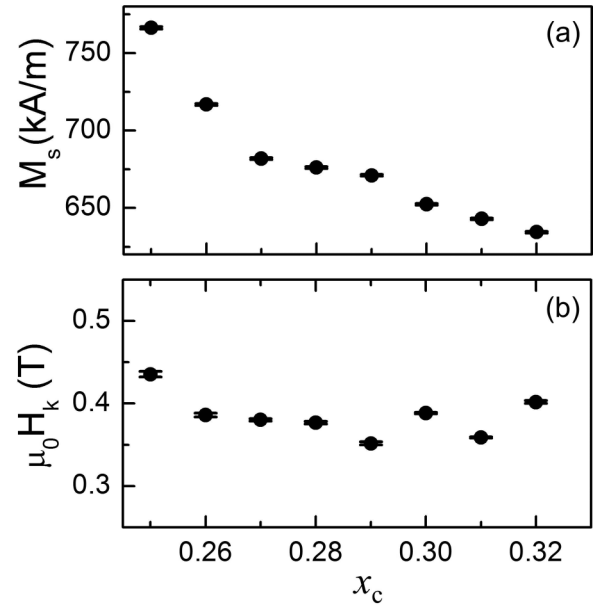


FIG. 5. Room temperature magnetic properties for the graded epitaxial Co/Co $_{1-x}$ Cr $_x$ /Co (10 $\bar{1}$ 0) samples as a function of Cr content x_c : (a) saturation magnetization M_S and (b) magnetocrystalline anisotropy field H_K .

exhibits a smaller “cone structure” around the HA than those of the graded samples. This corresponds to a lower anisotropy field H_K (defined as $H_K = 2(K_1 + 2K_2)/\mu_0 M_S$ [42]) for the pure Co sample, which is related to a growth-induced strain release with the thickness [43]. Nevertheless, the $M(H, \beta)$ data exhibit only minor quantitative variations upon changing the alloy composition, which means that the anisotropy symmetry and the easy axis orientation are neither impacted by the Cr concentration nor by the compositional gradient structure. In order to extract the volume-averaged magnetic properties, specifically, the anisotropy fields H_K and the saturation magnetizations M_S as a function of x_c , least-squares fits of the entire (not normalized) data sets have been performed by using a macrospin model [38]:

$$E = -\mu_0 M_S H \cos(\beta - \alpha) + K_1 \sin^2 \alpha + K_2 \sin^4 \alpha, \quad (1)$$

where α , the angle defined by the magnetization direction with respect to the easy axis, is numerically determined by energy minimization for each (H, β) pair [44]. The saturation magnetization, first- and second-order magnetocrystalline anisotropy constants, respectively, K_1 and K_2 [45], are the only fit parameters used for each of the not-normalized magnetization maps. The resulting fits [Figs. 4(f)–4(l)] exhibit excellent agreement with the experimental data [Figs. 4(a)–4(e)], with an average R^2 value of 0.975. The room temperature saturation magnetization M_S values, extracted from the fits, are shown in Fig. 5(a) as a function of x_c . As expected, M_S decreases upon increasing the Cr content [34–36]. At the same time, uniform Co $_{1-x}$ Cr $_x$ alloy samples with $x = 0.27$ or larger are expected to be no longer ferromagnetic at RT [34,46]. The reason why the extracted M_S values plotted in Fig. 5(a) do not drop down to zero in the high- x_c regime is due to the saturation magnetization of the two Co layers on the top and

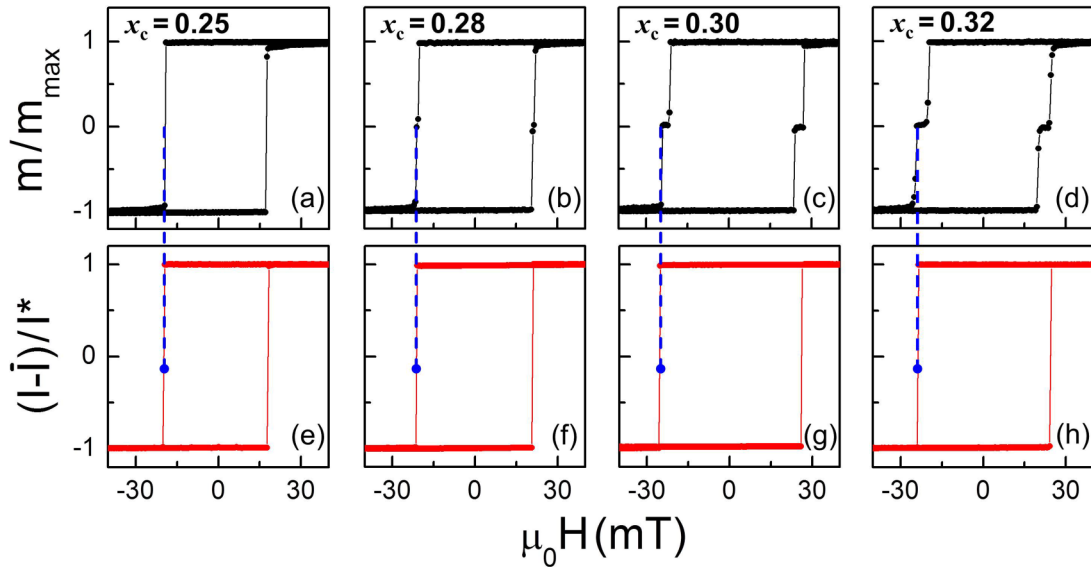


FIG. 6. (a–d) VSM room temperature magnetic moment vs field measurements along the easy axes for four different samples with Cr concentrations x_c . Hereby, the data are normalized to its maximum value m_{\max} in each case. (e–h) The corresponding MOKE measurements in direct comparison, which were acquired by using the same sample geometry and field resolution. The dashed (blue) lines are guides to the eye to compare the magnetic switching fields in between these two types of measurements. The MOKE data are processed in each case by first subtracting $\bar{I} = (I_{\max} + I_{\min})/2$ and then the resulting difference has been normalized by $I^* = (I_{\max} - I_{\min})/2$.

bottom of the structure, which are essentially not influenced by the compositional gradient. Thus, the total volume-averaged moment has a lower bound given by the M_S of the pure Co layers times their volume fraction.

The x_c dependence of the H_K is plotted in Fig. 5(b). It shows that the anisotropy field [42] is nearly independent of the graded film concentration. The reduction of K_1 and K_2 upon increasing x_c is very similar to the decrease of M_S with x_c , which implies that H_K should remain nearly constant in the entire concentration range. Therefore, despite the strongly depth-dependent compositional structure present in our samples, all of them exhibit a well-defined uniaxial magnetic anisotropy.

The remainder of our magnetometry investigation focused on the magnetization reversal processes occurring in these graded film structures. Figures 6(a)–6(d) show room temperature EA hysteresis curves for four selected samples, measured via VSM. In Fig. 6(a) the measurement shows a perfectly square-shaped hysteresis loop for the $x_c = 0.25$ sample, with an abrupt magnetization reversal at the switching field H_S , which in this particular case coincides with the coercive field H_C . In contrast, Fig. 6(b) displays a hysteresis loop in which the reversal of the magnetization occurs in two steps, similar to the reversal of two separated magnetic layers with distinct switching fields [47]. Figures 6(c) and 6(d) show that the difference between the two H_S 's increases progressively with x_c while the full remanence is preserved after positive and negative saturation. Intriguingly, the volume-averaged magnetization equals zero after the first reversal. Given the symmetry of the structure and the uniqueness of the switching fields, this intermediate state must correspond to a stable antiparallel magnetic configuration of the top and bottom half parts of the samples with one half reversing before the other to produce zero net magnetization.

While VSM and SQUID both yield volume-averaged magnetization, MOKE measurements provide information about the top part of the sample due to the typical penetration depth of visible light in metals that is only tens of nanometers, less than half of our symmetric structure's total thickness [40,48]. Thus, magneto-optical (MO) measurements have been performed in order to have comparative measurements and to gain deeper insights into the reversal process. Figure 6(e) displays the MOKE loop for the $x_c = 0.25$ sample along the EA. The measurement shows that the reversal between the two uniform magnetization states occurs via a single abrupt transition at the same value of the magnetic field measured for the entire sample via VSM. This confirms that for the $x_c = 0.25$ sample the magnetic correlation throughout the sample is so strong that the entire system switches collectively, even in the presence of the depth-dependent concentration gradient. Since the $x_c = 0.25$ alloys are themselves ferromagnetic at room temperature, $T_C \approx 420$ K [34], which is higher than the highest temperature used in our study, ferromagnetic coupling in and between all layers of the sample is expected. However, a discrepancy emerges between the MOKE and VSM measurements for $x_c \geq 0.28$. As shown in Figs. 6(f)–6(h), single-step transitions from positive saturation to negative saturation are always measured by MOKE, revealing that the surface switches as a single magnetic layer. In contrast, the VSM data for these samples show two-step reversal. As can be seen from the dashed (blue) lines in Fig. 6, the single-step transition observed via MOKE corresponds to the second switching field revealed by the VSM. This means that the bottom halves of all samples with $x_c \geq 0.28$ switch at lower fields and the top halves at higher fields. It is likely that the different switching fields for the top and bottom halves arise from different strain fields within the layers, e.g., as a result of symmetry breaking at the Cr/Co and Co/SiO₂ interfaces. Together, these measurements

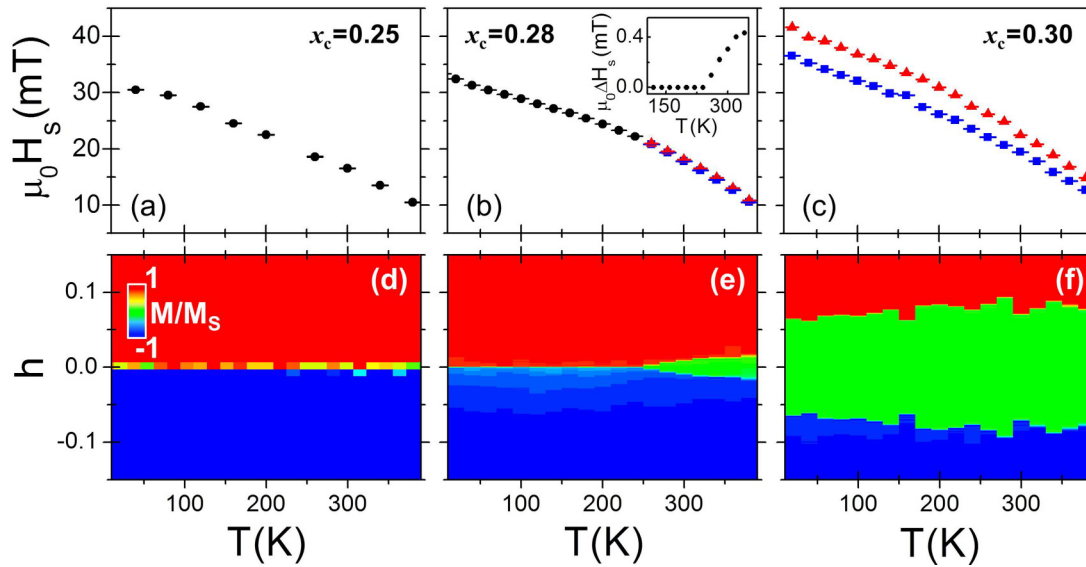


FIG. 7. (a–c) Switching field vs temperature for $x_c = 0.25, 0.28,$ and 0.30 . The (black) circles indicate “one-step” reversal, while the (blue) squares and (red) triangles indicate the values for two-step behavior. The inset in the central top panel shows the difference between the two H_s fields for the $x_c = 0.28$ sample as a function of temperature. (d–f) Color-coded maps of the field-dependent magnetization as a function of temperature measured along the easy axis for the hysteresis loop branches with decreasing field strengths. The individual figures on the top and the bottom correspond to the same sample each. The data are normalized to the saturation magnetization M_S , i.e., M/M_S equal to 1 represents positive magnetic polarization (red color), while -1 expresses negative saturation (blue color). The expected Curie temperatures for each doping concentration, based on literature data, are $T_C \approx 420$ K(a,d), $T_C \approx 270$ K(b,e), $T_C \approx 30$ K(c,f).

imply that when x_c is sufficiently large, the samples are not correlated throughout the thickness, with the top layer switching independently from the bottom layer.

The loss of ferromagnetic coupling between the top and bottom magnetic layers is expected when the central $\text{Co}_{1-x_c}\text{Cr}_{x_c}$ layer is approaching or is already in its paramagnetic state; otherwise the coupling should be strong. Therefore, a strong dependence on temperature should exist, which controls the magnetic phase at the center of the structure.

Temperature-dependent $M(H)$ measurements were thus performed in order to explore the possibility of observing a temperature-driven transition between a fully correlated and partially correlated magnetic structure. Figure 7(a) displays H_s as a function of temperature for the $x_c = 0.25$ sample. Single switching behavior of the magnetization is observed in the entire temperature range explored, despite the presence of a compositional gradient in the sample, consistent with the fact that the expected T_C of the $x = 0.25$ central layer alloy is higher than the highest measured temperature [34]. Moreover, $H_s(T)$ behaves as expected for a “single-layer material” for which K_1 increase upon lowering the temperature and thermally assisted switching is reduced.

In contrast, the $x_c = 0.30$ sample shown in Fig. 7(c) exhibits two-step reversal for all temperatures down to the lowest temperature that is accessible by our experimental setup, compatible with the expected T_C for the central layer, which is predicted to be close to 0 K [46]. As before, the reduction of the thermal energy leads to a shift towards higher values for the two switching fields connected to the top and bottom halves of the structure, but both shift in a similar fashion, so that a two-step reversal process persists for all temperatures. On

the other hand, an intermediate $x_c = 0.28$ exhibits two-step switching above $T = 260$ K, but one-step reversal below this “transition” temperature, as seen in Fig. 7(b). The inset shows the temperature dependence of the difference between the two switching fields H_s , which seems to follow a critical type behavior [49,50]. It is worth noting that $x = 0.28$ uniform alloy samples have been reported to exhibit $T_C \approx 270$ K [34], which is in very good quantitative agreement with the measured transition from one- to two-step reversal behavior observed at $T \approx 260$ K.

In order to better visualize the different switching regimes, Figs. 7(d)–7(f) display normalized magnetization M/M_S color-coded maps as a function of temperature and the reduced field $h = (H - \bar{H}_S)/\bar{H}_S$, with \bar{H}_S being the average of the two switching fields. Figure 7(d) illustrates that one-step magnetization switching occurs for all the temperatures explored for $x_c = 0.25$, highlighted by the presence of only two uniformly colored areas, whereas Fig. 7(f) shows in the same temperature range the constant presence of an intermediate magnetization state with $M/M_S = 0$ (marked by the green color) for $x_c = 0.30$. The transition between the two different regimes can be clearly seen in Fig. 7(e), where the two-step reversal, indicated by the triangular-shaped (green) area, disappears at $T = 260$ K. The data in Fig. 7 demonstrate two things. First, we can continuously tune the magnetization reversal mechanism by means of the alloy composition in graded structures, which allows the control of the effective exchange strength and thus the magnetic correlation along the surface normal. Second, choosing the concentration profile appropriately allows us to engineer a graded system that can undergo a transition from a collective one-step to a two-step reversal as a function of temperature.

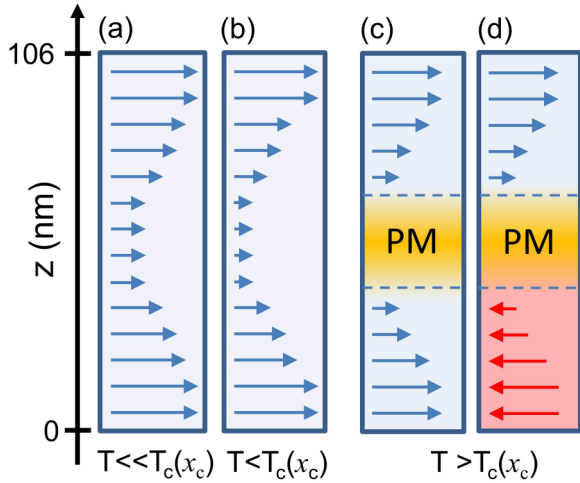


FIG. 8. Schematics of the magnetization depth profile at remanence for temperatures below (a,b) and above (c,d) the minimum effective T_C . For high temperatures, the paramagnetic (PM) region interrupts the exchange coupling through the thickness, allowing the system to be in either a parallel (c) or antiparallel (d) configuration.

In Fig. 8, we depict a schematic of the corresponding evolution of the magnetic depth profile for the $x_c = 0.28$ sample that would explain our observations. We consider our compositionally graded sample to constitute an exchange-coupled multilayer system, in which each layer develops a temperature-dependent magnetization that is determined by an effective Curie temperature associated with its local composition. Following the designed sample structure, the middle layer has the lowest exchange coupling J , M_S , and effective T_C , and hence it is the layer most sensitive to temperature changes. When the temperature is below the effective T_C of this layer [Figs. 8(a) and 8(b)], the system exhibits a depth-dependent M profile which does not go to zero even in the center of the structure and thus still behaves

like a single magnetic entity. Once the temperature crosses the minimum effective T_C of the $\text{Co}_{1-x_c}\text{Cr}_{x_c}$ layer, the structure essentially breaks into two magnetic entities, as shown in Fig. 8(c). In this case, the magnetizations of the top and bottom regions do not have to be correlated, allowing an external magnetic field to set the structure into an antiparallel alignment, if they have distinct switching fields [Fig. 8(d)]. It is worth pointing out that it would be possible to achieve the antiparallel configuration by forming a magnetic domain wall when $T < T_C(x_c)$. However, this state actually does not form during the magnetization reversal if T is sufficiently smaller than $T_C(x_c)$, because the energy of this domain wall state is too high and it does not represent an accessible magnetic state of the system. Instead, the reversal proceeds through a possible transient domain wall state, while only parallel states occur as nontransient magnetic states.

C. Polarized neutron reflectometry

1. Magnetic depth profile

Given the impracticability of probing the existence of the magnetic depth structure in our samples and its suggested evolution by using standard magnetometry techniques, the direct measurement of the depth-dependent magnetic profile and its temperature dependence has been performed by polarized neutron reflectometry.

Depth-dependent magnetic profiles of the $x_c = 0.28$ sample were obtained by PNR measurements as a function of temperature and magnetic field. After positively saturating the sample along the easy axis, non-spin-flip measurements, in which the original neutron polarization is preserved, were conducted in a near-remanent field $\mu_0 H = +1$ mT over a temperature range of $4 \text{ K} \leq T \leq 300 \text{ K}$. As an example, Fig. 9(a) shows the R^{--} and R^{++} data measured at $T = 4 \text{ K}$ as well as their associated model fit. The data exhibit spin-dependent oscillations generated by constructive and destructive interference as a function of Q_z , which indicates

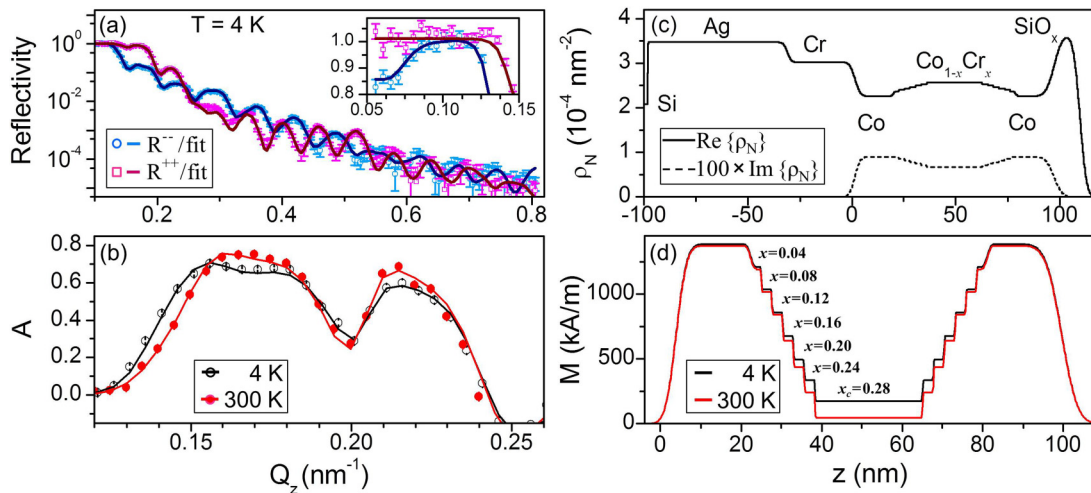


FIG. 9. (a) Fitted PNR data for $x_c = 0.28$ measured at $T = 4 \text{ K}$ in $\mu_0 H = 1 \text{ mT}$ along the easy axis following prior saturation via a $\mu_0 H = 700 \text{ mT}$ field; inset highlights low- Q_z spin splitting originating from the imaginary component of the Co scattering length density. (b) Low- Q_z fitted PNR spin asymmetry data measured in $\mu_0 H = 1 \text{ mT}$ at $T = 4 \text{ K}$ (open, black) and $T = 300 \text{ K}$ (filled, red). (c) Nuclear scattering length density model used to fit data at all field and temperature conditions. (d) Magnetization depth profile used to fit the data at $T = 4 \text{ K}$ (black) and $T = 300 \text{ K}$ (red). Error bars correspond to ± 1 standard deviation.

sensitivity to nuclear and magnetic depth profiles. Since the difference between the R^{--} and R^{++} signals scales with the component of the in-plane magnetization parallel to H , the magnetic contribution to the data can be highlighted by plotting the spin asymmetry A :

$$A = \frac{R^{(++)} - R^{(--)}}{R^{(++)} + R^{(--)}}. \quad (2)$$

The low- Q_z spin asymmetry values at $T = 4$ K and 300 K and their model fits are shown in Fig. 9(b). Since the Co layers provide the dominant contribution to this signal, and their magnetizations are only slightly reduced over this temperature range, the $T = 4$ K and $T = 300$ K spin asymmetries are overall rather similar. However, close inspection reveals definitive differences, demonstrating sensitivity to the temperature dependence of the magnetic depth profile. The data at all temperatures were well fit by the nuclear profile shown in Fig. 9(c). The nuclear scattering length density is defined as

$$\rho_N = \sum_i N_i b_i, \quad (3)$$

where N is the number density and b is the scattering length, with the summation being done over each isotope in the system. The nuclear profile was highly constrained, using only the nominal x profile for the $\text{Co}_{1-x}\text{Cr}_x$ multilayer [Fig. 9(c)] and literature values for N and b [51,52]. We note that ρ_N is complex for Co, although the imaginary component is more than 2 orders of magnitude smaller than the real component. This small complex component is accounted for in the model and leads to a distinguishing dip in R^{--} below the critical edge, as shown in the inset of Fig. 9(a). Magnetic profiles used to fit the data measured at $T = 4$ K and 300 K are shown in Fig. 9(d). The magnetic profiles were assumed to be spatially symmetric with respect to the central “mirror plane” of the graded structure, with the Co magnetization and the magnetizations of four intermediate $\text{Co}_{1-x}\text{Cr}_x$ profile values being utilized as free parameters, specifically the ones for the profile segments with $x = 0.04, x = 0.12, x = 0.20$, and $x = 0.28$. The magnetizations of the intermediate $x = 0.08, x = 0.16$, and $x = 0.24$ layers were constrained to be the average of the neighboring layer magnetizations to limit the number of free model parameters. As expected, the profiles show little change in the outer Co layers between $T = 4$ K and 300 K, and a progressively larger difference with increasing x down to the central $\text{Co}_{0.72}\text{Cr}_{0.28}$ layer, which exhibits the strongest reduction in magnitude upon T increase. The fits corresponding to the profiles displayed in panels (c) and (d) are exactly the ones shown as solid lines in panels (a) and (b). The fact that such a restricted model fits the data so well, even the low- Q_z feature corresponding to the imaginary ρ_N of Co, indicates the appropriateness of the model, which in turn corroborates that the intended compositional and magnetization depth structure was indeed achieved.

The depth distribution of the effective magnetizations and its change with temperature is illustrated in Fig. 10, where the temperature-dependent remnant magnetic profiles are summarized for the $\text{Co}_{1-x}\text{Cr}_x$ sublayers of the $x_c = 0.28$ sample. For Co and $\text{Co}_{1-x}\text{Cr}_x$ up to $x = 0.12$, the magnetization is basically temperature independent over the measured range. However, the $x = 0.20$ layer shows significant deviations at $T = 200$ K

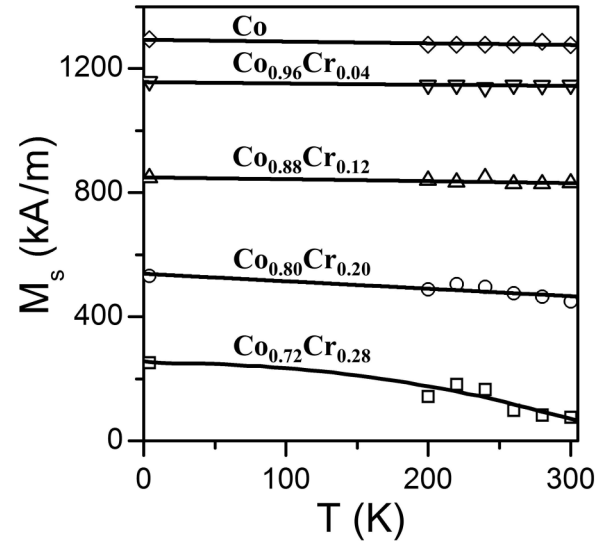


FIG. 10. Temperature dependence of the saturation magnetization for layers in the bathtub structure as determined from PNR for the sample with Cr concentration $x_c = 0.28$. Solid curves are guides to the eye. The open symbols include the error bars corresponding to ± 1 standard deviation.

and above, while the $x_c = 0.28$ curve falls off dramatically upon increasing T . These measurements demonstrate that the effective Curie temperature is indeed changing throughout the bathtub structure, with the outermost layers having the highest inherent ordering temperature, while the lowest effective T_C , close to room temperature, is located in the center of the sample. This result corroborates the physical picture suggested by the magnetometry study that revealed a transition from a square hysteresis loop one-step reversal at low temperatures to a two-step reversal just below $T = 300$ K.

2. Incoherent scattering model

In order to investigate temperature-dependent changes in the reversal behavior, field-dependent PNR measurements were conducted at several temperatures. At each temperature studied, the sample was first negatively saturated in an applied field $\mu_0 H = -0.7$ T, and subsequently, PNR spectra were measured at several positive fields near the switching of the magnetization. Typically, specular PNR is modeled under the assumption that the measured signal is *coherent*, i.e., the spatial extent of in-plane features is small enough that the reflectivity corresponds to a single average in-plane sample structure. However, very close to the switching of the magnetization, we found that our data could not be modeled in this way. As shown in Fig. 11, there is very little difference between the non-spin-flip reflectivities R^{--} and R^{++} , which within the coherent limit would suggest that the in-plane magnetization along H has dropped to zero. However, attempting to model these data with the known nuclear model from Fig. 9 and zero magnetization results in a grossly incorrect fit. Even treating each layer magnetization as a free parameter, it results in the unacceptably poor fit to the data that is shown in Fig. 11, which corresponds to the implausible magnetic profile shown in the inset. Nonspecular scans taken at several values of Q_z gave no

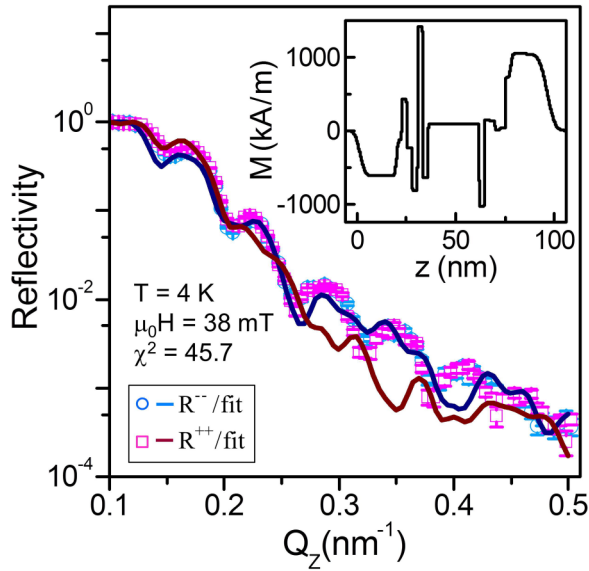


FIG. 11. PNR data measured at $T = 4$ K in $\mu_0 H = 38$ mT following prior saturation in a $\mu_0 H = -700$ mT for the sample with Cr concentration $x_c = 0.28$. Solid lines are best fits corresponding to a model assuming coherent scattering from a single magnetic depth profile (shown inset). Error bars correspond to ± 1 standard deviation.

evidence of increased diffuse scattering that might invalidate the implicit assumption of specular scattering.

Since we know the nuclear model determined from the remnant scans cannot change as a function of magnetic field, we consider the possibility of magnetic domains that are large enough for the measured signal to be *incoherent*, which means we are simultaneously measuring reflectivities corresponding to distinct depth profiles. This type of modeling is challenging, as without significant constraints on the individual domain profiles, the number of free parameters can become prohibitively large, rendering the results meaningless. Thus, we have chosen to use an extremely restrictive model based on information already determined from the previously discussed temperature-dependent remnant scans. The nuclear profile is fixed, as are the temperature-dependent magnetizations of the individual layers. The data are then modeled as an incoherent addition of reflectivities from only three domains: parallel positive (+), antiparallel (AP), and parallel negative (−). In doing so, the only free parameters are the relative fractional populations of the three domains [53]. Since the sum of these populations must add up to 1, this corresponds to only two free parameters per field condition. Figure 12(a) shows the magnetization depth profiles at $T = 4$ K for the three domain types that are being used to fit all field-dependent reflectivities measured at the same temperature, of which some are shown in Figs. 12(b)–12(d). Following negative saturation, at $\mu_0 H = 2$ mT the non-spin-flip scattering [Fig. 12(b)] is almost exactly spin transposed with respect to the scattering observed at $\mu_0 H = 1$ mT following positive saturation [Fig. 9(a)], i.e., R^{--} now looks like R^{++} and vice versa. This implies that the sample is uniformly negatively magnetized. This conclusion is borne out by the model fitting, which indicates 99% of the domains are in the negatively magnetized state and results in a good fit to the data. As the field is increased to

$\mu_0 H = 38$ mT [Fig. 12(c)], we encounter the near-coercivity state whose reflectivity could not be fit with a *coherent* model (Fig. 11). However, our *incoherent* modeling approach leads to an excellent fit to the data, which allows us to estimate nearly even populations of positive and negative domains. Notably, there is no antiparallel domain population at this condition. As the field is increased to $\mu_0 H = 41$ mT [Fig. 12(d)], the non-spin-flip reflectivities reverse with respect to Fig. 12(b), and the data are consistent with an essentially uniform positive magnetization. The magnetization depth profiles at $T = 298$ K are shown in Fig. 12(e) for the three possible domain states, with corresponding reversal data shown in panels Figs. 12(f)–12(h). Again, the $\mu_0 H = 2$ mT data [Fig. 12(f)] are fit well by a uniformly negatively magnetized sample. At $\mu_0 H = 21$ mT [Fig. 12(g)], near the coercive field, we see that the reversal mechanism is different than observed at low temperature, as the antiparallel state dominates the population. At $\mu_0 H = 25$ mT [Fig. 12(h)], the sample has returned to the positively saturated state.

The overall magnetization reversal results of our PNR measurements are summarized in Figs. 13(a)–13(d), which show the field-dependent domain populations at several temperatures. While all four temperatures exhibit multidomain states near the reversal, the antiparallel domain becomes more prominent as the temperature is increased. Thus we unambiguously demonstrate that the $x_c = 0.28$ graded sample features completely coupled reversal throughout the entire layer thickness at $T = 4$ K, while domains that exhibit independent reversal of the top and bottom of the bathtub structure progressively occur as the temperature approaches the effective local Curie temperature of the central layer. Moreover, it is worth mentioning that in our experiments only very weak spin-flip scattering is detected. This implies that the magnetization stays essentially collinear with the magnetic field along the easy axis throughout the reversal process. This is in agreement with our quantitative model.

Another important question is whether or not it is plausible to have magnetic domains large enough to justify our choice of an incoherent scattering model. For this, we consider the neutron beam in terms of wave packets with coherent extent Δr perpendicular the direction of propagation, a quantity known to be of order $1 \mu\text{m}$ for the PBR beamline [54]. We define the y direction to be the in-plane sample direction parallel to H , and x to be the in-plane sample direction perpendicular to H . In order for domains in the x - y plane of the sample to produce incoherent scattering, the spatial extent of those domains must be larger than L_x and L_y , i.e., the projections of Δr onto the sample surface. In our scattering geometry, H is applied perpendicular to the neutron propagation direction, so L_y is exactly equal to Δr . Along the x direction, neutrons are incident on the sample at a small angle with respect to the sample surface, stretching out L_x . Assuming Δr is $1 \mu\text{m}$ (a reasonable assumption based on Ref. [54]), our scattering geometry leads to $L_y = 1 \mu\text{m}$, and L_x that varies from $265 \mu\text{m}$ at $Q_z = 0.1 \text{ nm}^{-1}$ to $53 \mu\text{m}$ at $Q_z = 0.5 \text{ nm}^{-1}$.

To confirm whether such large domains emerge during reversal, we performed room temperature MOKE microscopy on the same $1 \text{ cm} \times 1 \text{ cm}$ square sample that the PNR measurement was performed on. We recorded videos of the magnetic domains at a frame rate of 24 s^{-1} while ramping the magnetic

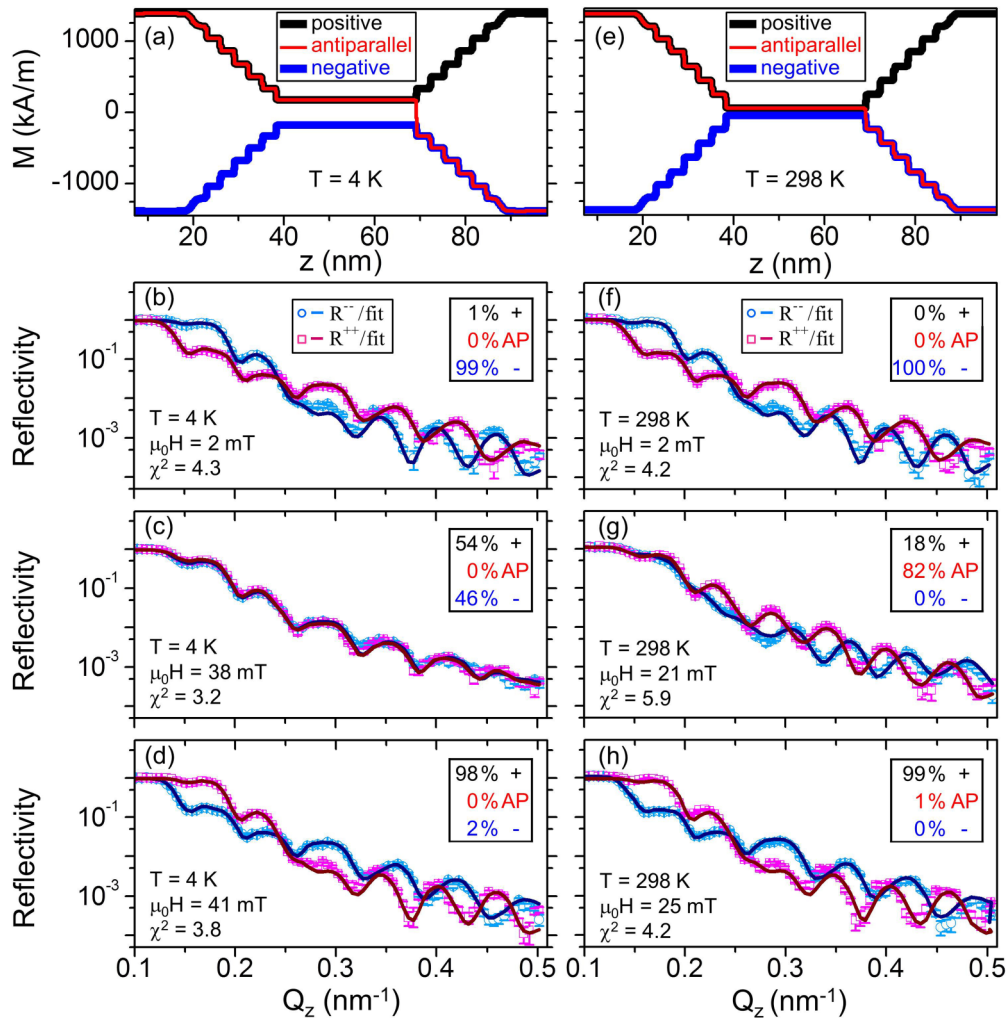


FIG. 12. Summary of incoherent model used to fit PNR data measured for the sample with Cr concentration $x_c = 0.28$ at $T = 4$ K and $T = 298$ K in increasing positive field following saturation in a $\mu_0 H = -700$ mT. (a) Three magnetic domains present in the $T = 4$ K model. (b-d) Fitted PNR data measured at $T = 4$ K in $\mu_0 H = 2$ mT, 38 mT, and 41 mT. (e) Domains for the $T = 298$ K magnetic model. (f-h) Fitted PNR data measured at $T = 298$ K in $\mu_0 H = 2$ mT, 21 mT, and 25 mT. Error bars correspond to ± 1 standard deviation.

field in the y direction at a rate of approximately 0.5 mT s^{-1} . We then selected a frame which shows a demagnetized state and subtracted it from an earlier frame which shows a saturated state, resulting in the high-contrast MOKE image in Fig. 13(e)

of the sample during the reversal process. In Fig. 13(e), a bright contrast indicates magnetization in the negative y direction, and dark contrast indicates magnetization in the positive y direction. The image was obtained with an applied

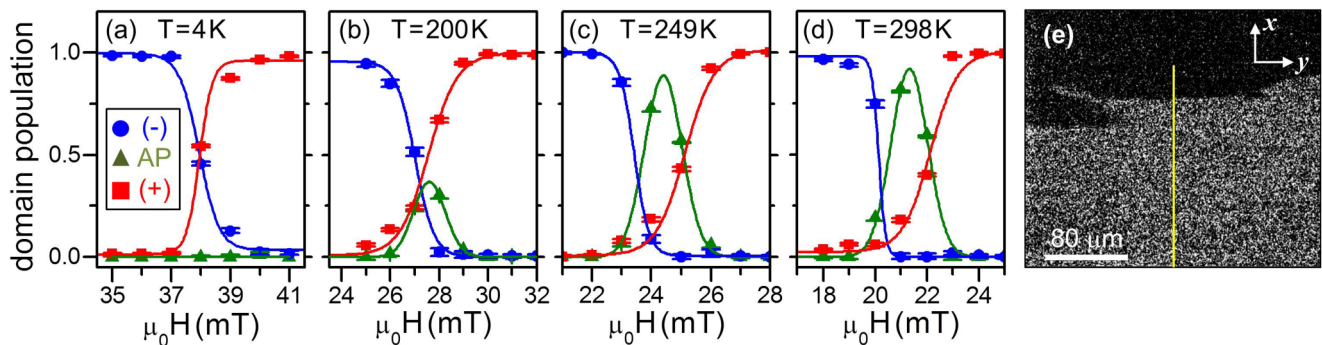


FIG. 13. (a-d) Field-dependent domain populations as determined from incoherent scattering model of the PNR data. Error bars correspond to ± 2 standard deviations. (e) Room temperature MOKE microscopy image taken during the reversal along the easy axis. Solid yellow line represents the average projection of the neutron coherence length for the PNR measurements.

field $\mu_0 H = 20.3$ mT. The thin yellow line corresponds to the average $L_x \times L_y$ illumination area for the entire Q_z range of the PNR experiment. The image clearly indicates that the magnetic domains in our samples are far larger than the entirety of the projection of a neutron wave packet on the sample surface. An *incoherent* model is therefore appropriate for describing our experimental PNR data. A more comprehensive model could incorporate the Q_z dependence of L_x , but such a model would add little to our evaluation of the reversal behavior of this system.

Considering these PNR results of the actual magnetization reversal process, there appears to be an inconsistency between the one-step reversal behavior deduced from low-temperature magnetometry data and the *incoherent* model introduced to analyze the PNR measurements, which requires the assumption of lateral domains. However, experimental details have to be considered to make this direct comparison. For the neutron characterization, $1\text{ cm} \times 1\text{ cm}$ square samples have been employed in order to achieve an optimal balance between data acquisition time and accessible Q_z range. On the other hand, in order to fit in between the pole pieces of the VSM electromagnet, an about 6 times smaller $4\text{ mm} \times 4\text{ mm}$ square sample segment had to be used. Furthermore, in both the VSM and the PNR setups, the static magnetic field generated by the magnets, and designed to be maximized and homogeneous at the exact center in between the poles, is not truly uniform for an extended sample. Therefore, a larger sample area introduces two superimposed and thus accumulative effects: a larger absolute inhomogeneity of the sample properties as well as larger variations of the external magnetic field throughout the sample volume. Therefore, the probability of creating lateral domain structures during the magnetization reversal increases most significantly with the sample size, which is the case for the PNR experiments in contrast to the VSM magnetometry data. Also, it has to be mentioned that the field range in which these domain states exist is very narrow, even in the case of the PNR measurements. Thus, the consistency of the experimental observations is not compromised by this very minor sample size-dependent effect.

IV. CONCLUSIONS

In summary, we have successfully fabricated epitaxial $\text{Co}/\text{Co}_{1-x}\text{Cr}_x/\text{Co}$ films with a compositional gradient of x that follows a bathtublike shape by means of sputter deposition. The epitaxial sample structure was determined, in-plane uniaxial anisotropy was verified, and the volume-averaged anisotropy constants measured. All the samples show uniaxial magnetic behavior, which allows us to study the compositional profile-induced effects in great detail. The sample set revealed a temperature- and composition-dependent magnetization reversal process. A fully correlated magnetic structure with one-step switching behavior was observed for temperatures below the effective Curie temperature of the central layer, whereas two-step switching was observed above this temperature. Specifically, $x_c \leq 0.25$ samples exhibit one-step switching for all temperatures measured, $x_c \geq 0.30$ samples show two-step switching for all temperatures measured, and $0.25 \leq x_c \leq 0.30$ samples have a temperature-dependent transition between one-step and two-step switching. The $x_c = 0.28$ sample

shows this transition at about 260 K, which is related to the magnetic ordering of the central $\text{Co}_{0.72}\text{Cr}_{0.28}$ layer at that temperature. We developed a detailed physical picture to explain the behavior of our samples and tested it quantitatively against our experimental results. Polarized neutron-scattering measurements confirmed the graded composition and effective Curie temperature depth profile. Moreover, due to the designed symmetric compositional graded structure, PNR experiments show the possibility to continuously shift the corresponding magnetization profiles towards or away from each other in the sample center, which in turn allows the temperature-dependent tunable correlation or decorrelation of the magnetic state and the magnetic reversal behavior. The neutron characterization corroborates the physical picture based on the magnetometry data, revealing that the intermediate state of the two-step reversal is indeed a state in which the top and bottom magnetizations are antiparallel aligned. Our results demonstrate the ability to design a ferromagnetic system that can be tuned from a collective to an individual reversal behavior, with the temperature being able to tune this correlation in a well-defined and predesigned manner. Practically, our findings prove that the operation point of a magnetic layer system from collective to localized behavior can be switched via temperature (or possibly by other stimuli), which should be interesting for tunable device technology in magnetic storage or spin-wave-based devices. Moreover, our results are notably consistent with the local T_C -profile picture, even on the nanometer-length scale, despite the collective nature of ferromagnetism. The exception to this is obviously the low-temperature collective reversal and the one-step to two-step transition, which cannot be explained by individual and independent (local) layers. Instead, the observed behavior means that if all sample regions are sufficiently ferromagnetic, only a collective reversal occurs, even if the parallel aligned magnetization profile is nonuniform and follows a local T_C profile. We believe these findings have practical consequences in that they give guidance to materials design for applications and micromagnetic calculations by demonstrating that down to the several nanometers length scale, many aspects of magnetic properties can be described and predicted by using a local property picture, including a local T_C description.

ACKNOWLEDGMENTS

We acknowledge support from the Basque Government under the Project No. PI2015_1_19 and from the Spanish Ministry of Economy and Competitiveness under Project No. FIS2015-64519-R (MINECO/FEDER). L.F. acknowledges support from the Predoctoral Program of the Basque Government through Grant No. PRE_2015_2_0126. M.P. acknowledges support from the Spanish Ministry of Economy and Competitiveness through Grant No. BES-2013-063690. P.R. acknowledges Obra Social “la Caixa” for her Ph.D. fellowship. C.W.M. acknowledges support initially and finally by NSF Grants No. 1522927 and No. 1609066, respectively. A.L.B. acknowledges support of this research under the Cooperative Research Agreement between the University of Maryland and the National Institute of Standards and Technology Center for Nanoscale Science and Technology, Award No. 70NANB10H193, through the University of

Maryland. We acknowledge John Unguris for use of the MOKE microscope. We thank Chuck Majkrzak of NIST for enlightening discussions on the nature of the neutron wave packet. Certain commercial equipment is identified in this paper to foster understanding. Such identification does not imply recommendation or endorsement by NIST, nor does it imply that the materials or equipment identified are necessarily the best available for the purpose.

APPENDIX: POLARIZED NEUTRON REFLECTOMETRY SETUP

PNR measurements were performed on the PBR beamline at the NIST Center for Neutron Research. A monochromatic wavelength $\lambda = 0.475$ nm cold neutron beam was incident on the sample surface, and the specular reflectivity was measured as a function of wave-vector transfer along the surface normal Q_z using a ^3He detector. An external magnetic field H was applied in the plane of the sample, and an Fe/Si supermirror/Al-coil spin flipper assembly was used to polarize the incident neutron magnetic moment either parallel (+) or antiparallel (−) to H . A second supermirror/flipper array was used to analyze the spin state of the scattered beam. The beam polarization was measured to be better than 90% for all polarization states. The data were corrected for background

(determined from measurements taken with the detector offset 0.3° from the specular condition), beam polarization, and beam footprint. Specular non-spin-flip (R^{--}, R^{++}) and spin-flip (R^{+-}, R^{-+}) reflectivities were measured under various field and temperature conditions [55,56]. The first and second superscripts denote the spin orientation of the incoming and scattered neutrons, respectively. PNR is sensitive to the sample's nuclear scattering length density $\rho_N(z)$ and the volume magnetization $M(z)$, with the z axis parallel to the surface normal. Specifically, non-spin-flip scattering $R^{++}(Q_z)$ and $R^{--}(Q_z)$ provide sensitivity on $\rho_N(z)$ and the in-plane component of $M(z)$ parallel to the applied external field H . Model fitting was performed using the NIST ReFlID software package [57], with parameter uncertainties determined using a Markov chain Monte Carlo algorithm [58,59]. Models used to fit the data feature discrete $\text{Co}_{1-x}\text{Cr}_x$ layers. While the measured Q_z range is sufficient to distinguish the “bathtub” structure, it does not provide significant sensitivity to the roughness in between the thin $\text{Co}_{1-x}\text{Cr}_x$ layers that make up the graded film segments. For simplicity in parameter interpretation, we chose a small value of 0.1 nm for this roughness (a choice that has no impact on our primary conclusions). Conversely, the underlayer roughnesses have been independently determined via free fitting parameters, since those layers are thicker.

-
- [1] R. E. Camley and R. L. Stamps, *J. Phys.: Condens. Matter* **5**, 3727 (1993).
- [2] I. Žutić, J. Fabian, and S. Das Sarma, *Rev. Mod. Phys.* **76**, 323 (2004).
- [3] C. A. Ramos, D. Lederman, A. R. King, and V. Jaccarino, *Phys. Rev. Lett.* **65**, 2913 (1990).
- [4] U. Bovensiepen, F. Wilhelm, P. Srivastava, P. Pouloupoulos, M. Farle, A. Ney, and K. Baberschke, *Phys. Rev. Lett.* **81**, 2368 (1998).
- [5] R. Skomski and D. J. Sellmyer, *J. Appl. Phys.* **87**, 4756 (2000).
- [6] M. Pärnaste, M. Marcellini, and B. Hjörvarsson, *J. Phys.: Condens. Matter* **17**, L477 (2005).
- [7] E. Kneller and R. Hawig, *IEEE Trans. Magn.* **27**, 3588 (1991).
- [8] J. Barnas, *Phys. Rev. B* **45**, 10427 (1992).
- [9] R. Skomski and J. M. D. Coey, *Phys. Rev. B* **48**, 15812 (1993).
- [10] E. E. Fullerton, J. S. Jiang, M. Grimsditch, C. H. Sowers, and S. D. Bader, *Phys. Rev. B* **58**, 12193 (1998).
- [11] E. E. Fullerton, J. S. Jiang, and S. D. Bader, *J. Magn. Magn. Mat.* **200**, 392 (1999).
- [12] D. C. Crew, J. Kim, L. H. Lewis, and K. Barmak, *J. Magn. Magn. Mater.* **233**, 257 (2001).
- [13] J. S. Jiang, J. E. Pearson, Z. Y. Liu, B. Kabius, S. Trasobares, D. J. Miller, S. D. Bader, D. R. Lee, D. Haskel, G. Srajer, and J. P. Liu, *J. Appl. Phys.* **97**, 10K311 (2005).
- [14] J. S. Jiang and S. D. Bader, *J. Phys.: Condens. Matter* **26**, 064214 (2014).
- [15] J. P. Wang, W. K. Shen, and J. M. Bai, *IEEE Trans. Magn.* **41**, 3181 (2005).
- [16] D. Suess, T. Schrefl, F. S. Fähler, M. Kirschner, G. Hrkac, F. Dorfbauer and J. Fidler, *Appl. Phys. Lett.* **87**, 012504 (2005).
- [17] R. H. Victoria and X. Shen, *IEEE Trans. Magn.* **41**, 537 (2005).
- [18] D. Suess, *Appl. Phys. Lett.* **89**, 113105 (2006).
- [19] A. Berger, N. Supper, Y. Ikeda, B. Lengsfeld, A. Moser, and E. E. Fullerton, *Appl. Phys. Lett.* **93**, 122502 (2008).
- [20] D. Suess, J. Fidler, G. Zimanyi, T. Schrefl, and P. Visscher, *Appl. Phys. Lett.* **92**, 173111 (2008).
- [21] D. Goll, A. Breitling, L. Gu, P. A. van Aken, and W. Sigle, *J. Appl. Phys.* **104**, 083903 (2008).
- [22] M. Morcellini, M. Pärnaste, B. Hjörvarsson, and M. Wolff, *Phys. Rev. B* **79**, 144426 (2009).
- [23] T. J. Zhou, B. C. Lim, and B. Liu, *Appl. Phys. Lett.* **94**, 152505 (2009).
- [24] B. J. Kirby, J. E. Davies, K. Liu, S. M. Watson, G. T. Zimanyi, R. D. Shull, P. A. Kienzle, and J. A. Borchers, *Phys. Rev. B* **81**, 100405 (2010).
- [25] B. J. Kirby, S. M. Watson, J. E. Davies, G. T. Zimanyi, K. Liu, R. D. Shull, and J. A. Borchers, *J. Appl. Phys.* **105**, 07C929 (2009).
- [26] V. Alexandrakakis, D. Niarchos, K. Mergia, J. Lee, J. Findler, and I. Panagiotopoulos, *J. Appl. Phys.* **107**, 013903 (2010).
- [27] J. S. Chen, L. S. Huang, J. F. Hu, G. Ju, and G. M. Chow, *J. Phys. D: Appl. Phys.* **43**, 185001 (2010).
- [28] V. Bonanni, Y. Fang, R. K. Dumas, C. Zha, S. Bonetti, J. Noguees, and J. Åkerman, *Appl. Phys. Lett.* **97**, 202501 (2010).
- [29] C. L. Zha, R. K. Dumas, Y. Fang, V. Bonanni, J. Noguees, and J. Åkerman, *Appl. Phys. Lett.* **97**, 182504 (2010).
- [30] R. K. Dumas, Y. Fang, B. J. Kirby, C. Zha, V. Bonanni, J. Noguees, and J. Åkerman, *Phys. Rev. B* **84**, 054434 (2011).
- [31] Y. Fang, R. K. Dumas, C. I. Zha, and J. Åkerman, *IEEE Magn. Lett.* **2**, 5500104 (2011).

- [32] C. Le Graët, T. R. Charlton, M. McLaren, M. Loving, S. A. Morley, C. J. Kinane, R. M. D. Brydson, L. H. Lewis, S. Langridge, and C. H. Marrows, *APL Mater.* **3**, 041802 (2015).
- [33] B. J. Kirby, H. F. Belliveau, D. D. Belyea, P. A. Kienzle, A. J. Grutter, P. Riego, A. Berger, and C. W. Miller, *Phys. Rev. Lett.* **116**, 047203 (2016).
- [34] S. Honda, K. Takahashi, and T. Kusuda, *Jap. J. Appl. Phys.* **26**, L593 (1987).
- [35] N. Inaba, M. Futamoto, and A. Nakamura, *IEEE Trans. Magn.* **34**, 1558 (1998).
- [36] N. Inaba, Y. Uesaka, and M. Futamoto, *IEEE Trans. Magn.* **36**, 54 (2000).
- [37] W. Yang, D. N. Lambeth, and D. E. Laughlin, *J. Appl. Phys.* **85**, 4723 (1999).
- [38] O. Idigoras, U. Palomares, A. K. Suszka, L. Fallarino, and A. Berger, *Appl. Phys. Lett.* **103**, 102410 (2013).
- [39] O. Idigoras, A. K. Suszka, P. Vavassori, B. Obry, B. Hillebrands, P. Landeros and A. Berger, *J. Appl. Phys.* **115**, 083912 (2014).
- [40] Z. Q. Qiu and S. D. Bader, *Rev. Sci. Instrum.* **71**, 1243 (2000).
- [41] P. Vavassori, *Appl. Phys. Lett.* **77**, 1605 (2000).
- [42] The anisotropy field H_K is defined as $H_K = 2(K_1 + 2K_2)/\mu_0 M_S$. The anisotropy constants K_1, K_2 and the room temperature saturation magnetization M_S are numerically determined using Eq. (1). The second-order anisotropy constant has been included here and in Eq. (1) since its value is well known to be relevant in Co-based material systems [45].
- [43] J. A. Arregi, J. B. Gonzalez-Diaz, O. Idigoras, and A. Berger, *Phys. Rev. B* **92**, 184405 (2015).
- [44] Both the magnetization M and the external applied field H lie in the $x - y$ plane perpendicular to the z axis, which is parallel to the sample surface normal.
- [45] M. Grimsditch, E. E. Fullerton, and R. L. Stamps, *Phys. Rev. B* **56**, 2617 (1997).
- [46] F. Bolzoni, L. Leccabue, R. Panizzieri, and L. Pareti, *J. Magn. Magn. Mater.* **31**, 845 (1983).
- [47] F. Ilievski, J. C. Perkinson, and C. A. Ross, *J. Appl. Phys.* **101**, 09D116 (2007).
- [48] R. Schäfer, *J. Magn. Magn. Mater.* **148**, 226 (1995).
- [49] A. Berger, A. Inomata, J. S. Jiang, J. E. Pearson, and S. D. Bader, *Phys. Rev. Lett.* **85**, 4176 (2000).
- [50] J. A. Arregi, O. Idigoras, P. Vavassori, and A. Berger, *Appl. Phys. Lett.* **100**, 262403 (2012).
- [51] I. S. Anderson, P. J. Brown, J. M. Carpenter, G. Lander, R. Pynn, J. M. Rowe, O. Schärpf, V. F. Sears, and B. T. M. Willis, *International Tables for Crystallography* (Wiley, Hoboken, NJ, 2006), Chap. 4.4, p. 430.
- [52] The ρ_N profile has been multiplied by a single scaling factor to account for variations in density due to alloying. This is a small effect, as the fitted value of the scaling factor is 1.03.
- [53] The maximum reflectivity and a small constant angular offset are also treated as free parameters to account for variations in alignment from scan-to-scan.
- [54] C. F. Majkrzak, C. Metting, B. B. Maranville, J. A. Dura, S. Satija, T. Udovic, and N. F. Berk, *Phys. Rev. A* **89**, 033851 (2014).
- [55] T. Chatterji, in *Neutron Scattering from Magnetic Materials* (Elsevier Science, New York, 2005), Chap. 9.
- [56] G. P. Felcher, *Physica B* **267**, 154 (1999).
- [57] B. J. Kirby, P. A. Kienzle, B. B. Maranville, N. F. Berk, J. Krycka, F. Heinrich, and C. F. Majkrzak, *Curr. Opin. Colloid. Interface Sci.* **17**, 44 (2012).
- [58] *In ISO/IEC Guide 98-3::2008/Suppl 1:2008, Propagation of Distributions Using a Monte Carlo Method*, 1st ed. (International Organization for Standardization, Geneva, Switzerland, 2008).
- [59] J. A. Vrugt, C. J. F. T. Braak, C. G. H. Diks, D. Higdon, B. A. Robinson, and J. M. Hyman, *Int. J. Nonlinear Sci. Numer. Simul.* **10**, 273 (2009).